A phase-field lattice Boltzmann method for the solution of water-entry and water-exit problems

DOI:
10.1111/mice.12651

Document Version
Accepted author manuscript

Received <day> <Month>, <year>; | Revised <day> <Month>, <year>; | Accepted <day> <Month>, <year>

DOI: xxx/xxxx

ORIGINAL ARTICLE

A phase-field lattice Boltzmann method for the solution of water-entry and water-exit problems

Alessandro De Rosis*[,1] | Angelantonio Tafuni[2]

[1]Department of Mechanical, Aerospace and Civil Engineering, The University of Manchester, Manchester, M13 9PL, United Kingdom

[2]School of Applied Engineering and Technology, New Jersey Institute of Technology, Newark, New Jersey 07103, USA

***Correspondence**

*Alessandro De Rosis, Oxford Rd, Manchester M13 9PL, United Kingdom.

Email: alessandro.derosis@manchester.ac.uk

Summary

In this paper, an original phase-field lattice Boltzmann scheme for a system composed of two immiscible and incompressible fluids interacting with moving solids is developed, presented and tested for the first time. The proposed approach is benchmarked against experimental data and Smoothed Particle Hydrodynamics simulations of four well-established two-dimensional problems where a rigid body interacts with the interface between the two fluids. The outlined methodology represents a very good candidate to perform fluid-structure interaction simulations of hydrodynamic stability problems as well as water-entry and water-exit problems.

KEYWORDS:

water entry; phase-field theory; lattice Boltzmann method; Smoothed Particle Hydrodynamics

1 | MOTIVATION

Phenomena of fluid-structure interaction (FSI) are ubiquitous in many areas of civil and offshore engineering. For example, a dam, as well as any other barrier for hydraulic protection, should be built in order to withstand the static forces exerted by the contained water. The role of FSI is even more important for offshore structures, where the solid body undergoes dynamic time-dependent fluid actions. Therefore, accurate predictions of fluid forces are instrumental to an effective design of such types of structures (Kühner, Crouse, Rank, Tölke, & Krafczyk (2004); Leonardi, Wittel, Mendoza, Vetter, & Herrmann (2016)), as well as fluid dampers (Balendra, Wang, & Cheong (1995); Colwell & Basu (2008); Gao, Kwok, & Samali (1997); Wang, Ni, Ko, & Spencer Jr (2005)). In order to achieve this goal, a very effective and consolidated tool is represented by numerical simulations of computational fluid dynamics (CFD), an area of fluid dynamics that has seen increasing interest from both academic and industrial researchers.

Traditionally, CFD simulations have been carried out by solving the Navier-Stokes equations with finite volume procedures. Despite its wide application, traditional CFD suffers from several problems particularly emphasized in the context of FSI analyses. For example, upon structure motion, the fluid mesh in traditional CFD methods may need to be re-generated at each time step, a process that can be very expensive computationally speaking. Notice that traditional CFD can use overset/chimera meshes, where high mesh detail can be used on the solid body and complex 3D problems can be solved with relative ease. This and other challenges (Manjula, Ariyaratne, Ratnayake, & Melaaen (2017); Velázquez & Castillo (2008); Zhu, Gu, & Chen (2007)) constitute the basis for researching more efficient algorithmic procedures.

In the last decades, the lattice Boltzmann method (LBM) has attracted a progressively larger attention as an alternative method to classical CFD (He & Luo (1997); Krüger et al. (2017)). Instead of solving the Navier-Stokes equations, the LBM is based on the Boltzmann equation. The computational domain is represented by a fixed Eulerian Cartesian lattice grid where the fluid is idealized by distributions of particles colliding and streaming along the links of this lattice. The LBM exhibits several distinctive advantages, as for example the simplicity of its mathematical formulation. Moreover, there is no need to solve the Poisson equation to calculate the pressure, as is done for incompressible Navier-Stokes solvers.

The outstanding popularity of LBM has been mainly

(though not exclusively) due by the simplicity of its collision operator, the Bhatnagar-Gross-Krook (BGK) one (Bhatnagar, Gross, & Krook (1954)), where distributions relax to a certain equilibrium state with a common unique rate. Despite its extensive adoption, the BGK approximation undergoes instabilities when challenging numerical simulations are undertaken, as for example those characterized by high-Reynolds-number and high-density-ratio flows. Indeed, this configuration is typical of water-entry and water-exit problems, where the Reynolds number and the density contrasts are usually very high. These limitations can be attributed to the concurrent presence of two factors: (i) the relaxation to a non-complete equilibrium state (Malaspinas (2015)) and the presence of non-hydrodynamic ghost modes (Latt & Chopard (2006)). In order to overcome these issues, a central-moments-based multiple-relaxation-time LBM has been proposed recently (De Rosis, Huang, & Coreixas (2019); De Rosis & Luo (2019)). Within this framework, the collision process is performed in the space of central moments (CMs) (Geier, Greiner, & Korvink (2006)), relaxing to a complete equilibrium (Coreixas, Wissocq, Puigt, Boussuge, & Sagaut (2017); Malaspinas (2015)) with different relaxation times, thus allowing the damping of non-hydrodynamic modes. When compared to the BGK approach, this new LB method shows the same accuracy but remarkably higher stability properties (De Rosis (2016 2017)).

In this paper, an original central-moments-based multiple-relaxation-time LBM for a system composed of two immiscible and incompressible fluids is presented and tested against experimental data and Smoothed Particle Hydrodynamics (SPH) (Monaghan (1992)) simulations of four well-consolidated two-dimensional problems where a rigid body interacts with the interface between the two fluids. While the flow physics is governed by the incompressible Navier-Stokes equations, the evolution of the interface obeys the Allen-Cahn equation. The adoption of CMs with respect to the BGK model is justified by numerical tests demonstrating that the former outperforms the latter in terms of stability. Numerical simulations herein prove that the new LB approach is an excellent candidate for predicting fluid-structure interaction phenomena when high-Reynolds-number and high-density-contrast flows are considered. When compared to the recent work by Dinesh Kumar, Sannasiraj, & Sundar (2019), our work shows two distinct features (see also Section 2.3): (i) the inclusion of the complete set of Hermite polynomials for all the equilibrium and forcing terms, and (ii) the use of central moments, instead or raw ones, in the collision operators. These allow us to run numerical simulations at a Reynolds number of order 10^6 as opposed to a Reynolds in the order 10^4 for cases in Dinesh Kumar et al. (2019), as well as to enhance the stability and accuracy of these types of simulations (see Appendix A for more details). Very recently, central moments have also been adopted by Gruszczyński, Mitchell, Leonardi, Laniewski-Wollk, & Barber (2019). With respect to this work, our approach is not based on the so-called cascaded LBM, where moments are built on the *continuous* equilibrium and forcing terms, but on a theoretical formulation where the *discrete* counterparts are adopted. As a consequence, the resultant algorithmic procedure is very general, can be extended to any lattice discretization and shows intelligible derivations and an easy practical implementation.

The reason behind the choice of Smoothed Particle Hydrodynamics as a validation tool is twofold: on the one hand, SPH is a fully Lagrangian meshless method that is known to handle free-surface and interfacial flow quite well, making it a good benchmark candidate. Several instances of using SPH for marine and offshore structure problems can be found in recent works (Crespo, Altomare, Domínguez, González-Cao, & Gómez-Gesteira (2017); Domínguez et al. (2019); Mogan, Chen, Hartwig, Sahin, & Tafuni (2018); Tafuni, Sahin, & Hyman (2016)). On the other hand, both LBM and SPH solve incompressible flow problems with a weakly-compressible hypothesis, making the pressure treatment similar and therefore allowing for a more consistent comparison of pressure outcomes between the two methods.

The rest of the paper is organized as follows. In Section 2, the modeling approach is outlined. Results from numerical tests are discussed in Section 3. Some conclusions are drawn in Section 4. Eventually, additional details about the computations presented in this work are given in Appendix.

2 | MODELLING APPROACH

In this section, we first state the macroscopic equations governing the system. Secondly, we summarize the BGK LBM in Fakhari, Mitchell, Leonardi, & Bolster (2017). Finally, we present our original LB approach based on central moments.

2.1 | Governing equations

Let us consider a system composed of two immiscible and incompressible fluids. The macroscopic behavior is governed by the Navier-Stokes equations:

$$\begin{aligned} \boldsymbol{\nabla}\cdot\mathbf{u} &= 0, \\ \rho\left[\partial_t\mathbf{u} + (\mathbf{u}\cdot\boldsymbol{\nabla})\,\mathbf{u}\right] &= -\boldsymbol{\nabla}p + \mu\boldsymbol{\nabla}^2\mathbf{u} + \boldsymbol{F}, \end{aligned} \tag{1}$$

where t is the time, $\mathbf{u}$ is the flow velocity, ρ is the density, p is the pressure, μ is the dynamic viscosity and $\boldsymbol{F}$ accounts for any external force. In order to track the interface between the two fluids, an additional equation must be solved. Specifically, here we consider the conservative form of the Allen-Cahn

equation Allen & Cahn (1976) proposed in Chiu & Lin (2011), that is

$$\partial_t \phi + \boldsymbol{\nabla} \cdot \phi \mathbf{u} = \boldsymbol{\nabla} \cdot M \left[\boldsymbol{\nabla} \phi - \frac{\boldsymbol{\nabla} \phi}{|\boldsymbol{\nabla} \phi|} \frac{1 - 4 \left(\phi - \phi_0 \right)^2}{\xi} \right], \quad (2)$$

where M is a mobility coefficient, ξ is the interface thickness, ϕ is the order parameter that varies between $\phi_H = 1$ for the heavier fluid and $\phi_L = 0$ for the lighter one, and $\phi_0 = \left(\phi_H + \phi_L \right) / 2$.

2.2 | BGK LBM

Let us consider a two-dimensional Cartesian space $\boldsymbol{x} = [x, y]$, where x and y denote the horizontal and vertical coordinates, respectively. In order to predict the behavior of a two-fluids system, two groups of particle distribution functions (or populations) are considered. The former, $|f_i\rangle = \left[f_0, f_1, f_2, f_3, f_4, f_5, f_6, f_7, f_8 \right]^\top$, controls the velocity field, while the latter, $|g_i\rangle = \left[g_0, g_1, g_2, g_3, g_4, g_5, g_6, g_7, g_8 \right]^\top$, monitors the evolution of the order parameter. Notice that $|\bullet\rangle$ denotes a column vector and the superscript $\top$ indicates the transpose operator. In the D2Q9 model (Succi (2001)), populations move on a fixed Cartesian square lattice along the generic link $i = 0 \dots 8$ with velocity $\mathbf{c}_i = [|c_{xi}\rangle, |c_{yi}\rangle]$ defined as $|c_{xi}\rangle = [0, 1, 0, -1, 0, 1, -1, -1, 1]^\top$ and $|c_{yi}\rangle = [0, 0, 1, 0, -1, 1, 1, -1, -1]^\top$. The governing LB equations reads as follows:

$$|f_i(\boldsymbol{x} + \boldsymbol{c}_i, t+1)\rangle = |f_i^\star(\boldsymbol{x}, t)\rangle, \quad (3)$$

$$|g_i(\boldsymbol{x} + \boldsymbol{c}_i, t+1)\rangle = |g_i^\star(\boldsymbol{x}, t)\rangle. \quad (4)$$

where the superscript $\star$ represents the so-called post-collision state. To lighten the notation, the dependence on space $\boldsymbol{x}$ and time t will be implicitly assumed in the rest of this section.

Within the BGK approximation (Bhatnagar et al. (1954)), post-collision populations can be computed as

$$f_i^\star = f_i + \frac{1}{\tau + 1/2} \left(f_i^{eq} - f_i \right) + F_i \quad (5)$$

$$g_i^\star = g_i + \frac{1}{\tau_\phi + 1/2} \left(g_i^{eq} - g_i \right) + G_i, \quad (6)$$

where the equilibrium states are

$$f_i^{eq} = w_i \left[\tilde{p} + \frac{\mathbf{c}_i \cdot \mathbf{u}}{c_s^2} + \frac{\left(\mathbf{c}_i \cdot \mathbf{u} \right)^2}{2 c_s^4} - \frac{\mathbf{u}^2}{2 c_s^2} \right], \quad (7)$$

$$g_i^{eq} = w_i \phi \left[1 + \frac{\mathbf{c}_i \cdot \mathbf{u}}{c_s^2} + \frac{\left(\mathbf{c}_i \cdot \mathbf{u} \right)^2}{2 c_s^4} - \frac{\mathbf{u}^2}{2 c_s^2} \right], \quad (8)$$

$\tilde{p} = p / (\rho c_s^2)$ being the normalized pressure and $\mathbf{u} = [u_x, u_y]$. The symbol $\cdot$ denotes the scalar product of two vectors. Weighting factors are $w_0 = 4/9$, $w_{1\dots4} = 1/9$, $w_{5\dots8} = 1/36$ and the lattice sound speed is $c_s = c/\sqrt{3}$, with $c = 1$ (Succi (2001)). The relaxation times are evaluated as

$$\tau = \tau_L + \frac{\phi - \phi_L}{\phi_H - \phi_L} \left(\tau_H - \tau_L \right), \qquad \tau_\phi = \frac{M}{c_s^2}, \quad (9)$$

where $\tau_L = \mu_L / (\rho c_s^2)$ and $\tau_H = \mu_H / (\rho c_s^2)$ are the relaxation times associated to the fluids of dynamic viscosities μ_L and μ_H, respectively. Notice that τ is computed by applying the linear interpolation proposed by Gruszczyński et al. (2019), that has been proved to be able to reduce spurious currents. According to Fakhari et al. (2017), the two forcing terms can be written as

$$F_i = w_i \frac{\mathbf{c}_i \cdot \boldsymbol{F}}{\rho c_s^2}, \qquad G_i = w_i \frac{\mathbf{c}_i \cdot \boldsymbol{F}_\phi}{c_s^2}. \quad (10)$$

where

$$\boldsymbol{F}_\phi = [F_{x,\phi}, F_{y,\phi}] = c_s^2 \frac{1 - 4 \left(\phi - \phi_0 \right)^2}{\xi} \cdot \frac{\boldsymbol{\nabla} \phi}{|\boldsymbol{\nabla} \phi|}, \quad (11)$$

$\boldsymbol{\nabla}$ being the gradient operator. The force $\boldsymbol{F} = [F_x, F_y]$ gathers four contributions:

$$\boldsymbol{F} = \boldsymbol{F}_s + \boldsymbol{F}_p + \boldsymbol{F}_\mu + \boldsymbol{F}_b. \quad (12)$$

$\boldsymbol{F}_s$ accounts for the surface tension as

$$\boldsymbol{F}_s = \mu_\phi \boldsymbol{\nabla} \phi, \quad (13)$$

with the chemical potential

$$\mu_\phi = 4\beta \left(\phi - \phi_L \right) \left(\phi - \phi_H \right) \left(\phi - \phi_0 \right) - \kappa \boldsymbol{\nabla}^2 \phi, \quad (14)$$

where $\beta = 12\sigma/\xi$ and $\kappa = 3\sigma\xi/2$, σ being the surface tension. Notice that the gradient and Laplacian operators of ϕ are computed by isotropic finite differences:

$$\boldsymbol{\nabla} \phi = \frac{1}{c_s^2} \sum_i w_i \mathbf{c}_i \phi(\boldsymbol{x} + \mathbf{c}_i),$$
$$\boldsymbol{\nabla}^2 \phi = \frac{2}{c_s^2} \sum_i w_i \left[\phi(\boldsymbol{x} + \mathbf{c}_i) - \phi(\boldsymbol{x}) \right]. \quad (15)$$

The pressure and viscous forces are

$$\boldsymbol{F}_p = -\tilde{p} c_s^2 \boldsymbol{\nabla} \rho, \qquad \boldsymbol{F}_\mu = \nu \left[\boldsymbol{\nabla} \mathbf{u} + (\boldsymbol{\nabla} \mathbf{u})^\top \right] \cdot \boldsymbol{\nabla} \rho, \quad (16)$$

respectively, where the fluid kinematic viscosity is $\nu = \tau c_s^2$. The gradient of density is determined based on the gradient of the order parameter, that is

$$\boldsymbol{\nabla} \rho = \frac{\rho_H - \rho_L}{\phi_H - \phi_L} \boldsymbol{\nabla} \phi. \quad (17)$$

The last term, $\boldsymbol{F}_b$, accounts for a generic body force (*e.g.* gravity).

Macroscopic variables are readily available as

$$\tilde{p} = \sum_i f_i, \quad \mathbf{u} = \sum_i f_i \mathbf{c}_i + \frac{\boldsymbol{F}}{2\rho}, \quad \phi = \sum_i g_i. \quad (18)$$

Eventually, the fluid density ρ is computed by a linear interpolation, that is

$$\rho = \rho_L + \frac{\phi - \phi_L}{\phi_H - \phi_L}\left(\rho_H - \rho_L\right). \tag{19}$$

2.3 | CMs-based LBM

Here, we discuss our proposed modelling approach, where the two collision processes in Eqs. (5,6) are executed in the space of central moments.

2.3.1 | CMs-based LBM for f_i

The post-collision populations can be written as

$$\begin{aligned}|f_i^\star(\boldsymbol{x},t)\rangle = |f_i(\boldsymbol{x},t)\rangle + \boldsymbol{\Lambda}[|f_i^{\mathrm{eq}}(\boldsymbol{x},t)\rangle - |f_i(\boldsymbol{x},t)\rangle] \\ + (\mathbf{I} - \boldsymbol{\Lambda}/2)\,|F_i(\boldsymbol{x},t)\rangle\,.\end{aligned} \tag{20}$$

The collision matrix is $\boldsymbol{\Lambda} = \mathbf{T}^{-1}\mathbf{K}\mathbf{T}$, where $\mathbf{K} = \mathrm{diag}[1, 1, 1, 1, \omega, \omega, 1, 1, 1]$ is the relaxation matrix, with $\omega = 1/(\tau + 1/2)$. $\mathbf{T}$ is a non-orthogonal basis of moments taking the form (De Rosis (2016)):

$$\begin{aligned}\mathbf{T} = \Big[&\langle|\boldsymbol{c}_i|^0|\,,\, \langle\bar{c}_{ix}|\,,\, \langle\bar{c}_{iy}|\,,\, \langle\bar{c}_{ix}^2 + \bar{c}_{iy}^2|\,,\, \langle\bar{c}_{ix}^2 - \bar{c}_{iy}^2|\,,\\ &\langle\bar{c}_{ix}\bar{c}_{iy}|\,,\, \langle\bar{c}_{ix}^2\bar{c}_{iy}|\,,\, \langle\bar{c}_{ix}\bar{c}_{iy}^2|\,,\, \langle\bar{c}_{ix}^2\bar{c}_{iy}^2|\Big]^\top,\end{aligned} \tag{21}$$

where $\langle\bar{c}_{ix}| = \langle c_{ix} - u_x|\,, \quad \langle\bar{c}_{iy}| = \langle c_{iy} - u_y|$ are the lattice directions by the local fluid velocity, with $\langle\boldsymbol{c}_i| = [\langle\bar{c}_{ix}|\,,\, \langle\bar{c}_{iy}|]$ (Geier et al. (2006)). $\langle\bullet|$ denotes a row vector.

The collision stage is performed in the space of central moments as follows:

$$|k_i^\star\rangle = (\mathbf{I} - \mathbf{K})\,|k_i\rangle + \mathbf{K}\,|k_i^{\mathrm{eq}}\rangle + \left(\mathbf{I} - \frac{\mathbf{K}}{2}\right)|R_i\rangle\,, \tag{22}$$

where pre-collision, equilibrium and post-collision CMs are gathered through the vectors $|k_i\rangle$, $|k_i^{\mathrm{eq}}\rangle$, and $|k_i^\star\rangle$, respectively. The first two quantities are evaluated by applying the matrix $\mathbf{T}$ to the corresponding distribution, that is $|k_i\rangle = \mathbf{T}\,|f_i\rangle\,, \quad |k_i^{\mathrm{eq}}\rangle = \mathbf{T}\,|f_i^{\mathrm{eq}}\rangle$. Instead of representing the equilibrium distribution by Eq. (7), we follow Malaspinas (2015) and Coreixas et al. (2017), where it has been shown that the full potential of the D2Q9 discretization can be exploited by expanding the equilibrium distributions into a basis of Hermite polynomials $\boldsymbol{\mathcal{H}}^{(n)}$ up to the fourth order in the D2Q9 space. Therefore, we can write

$$\begin{aligned}f_i^{\mathrm{eq}} = w_i\Bigg[&\tilde{p} + \frac{\boldsymbol{\mathcal{H}}_i^{(1)}\cdot\mathbf{u}}{c_s^2} + \frac{1}{2c_s^4}\boldsymbol{\mathcal{H}}_i^{(2)} : \mathbf{uu}\\ &+\frac{1}{2c_s^6}\left(\boldsymbol{\mathcal{H}}_{ixxy}^{(3)}u_x^2u_y + \boldsymbol{\mathcal{H}}_{ixyy}^{(3)}u_xu_y^2\right) + \frac{1}{4c_s^8}\boldsymbol{\mathcal{H}}_{ixxyy}^{(4)}u_x^2u_y^2\Bigg],\end{aligned} \tag{23}$$

where

$$\begin{aligned}\mathcal{H}_{ix}^{(1)} &= c_{ix}, \qquad \mathcal{H}_{iy}^{(1)} = c_{iy},\\ \mathcal{H}_{ixx}^{(2)} &= c_{ix}^2 - c_s^2, \quad \mathcal{H}_{iyy}^{(2)} = c_{iy}^2 - c_s^2, \quad \mathcal{H}_{ixy}^{(2)} = c_{ix}c_{iy},\\ \mathcal{H}_{ixxy}^{(3)} &= \left(c_{ix}^2 - c_s^2\right)c_{iy}, \quad \mathcal{H}_{ixyy}^{(3)} = \left(c_{iy}^2 - c_s^2\right)c_{ix},\\ \mathcal{H}_{ixxyy}^{(4)} &= \left(c_{ix}^2 - c_s^2\right)\left(c_{iy}^2 - c_s^2\right).\end{aligned} \tag{24}$$

To obtain the central moments of the forcing term $|R_i\rangle = \mathbf{T}\,|F_i\rangle$, we employ the expression adopted in Huang, Wu, & Adams (2018), with Hermite polynomials of the maximum admissible order (i.e., four):

$$\begin{aligned}F_i = w_i\Bigg(&\frac{\boldsymbol{F}}{\rho c_s}\cdot\hat{\boldsymbol{\mathcal{H}}}^{(1)} + \frac{[\boldsymbol{F}\mathbf{u}]}{2\rho c_s^2}\cdot\hat{\boldsymbol{\mathcal{H}}}^{(2)}\\ &+\frac{[\boldsymbol{F}\mathbf{uu}]}{6\rho c_s^3}\cdot\hat{\boldsymbol{\mathcal{H}}}_{[xyy],[xxy]}^{(3)} + \frac{[\boldsymbol{F}\mathbf{uuu}]}{24\rho c_s^4}\cdot\hat{\boldsymbol{\mathcal{H}}}_{[xxyy]}^{(4)}\Bigg),\end{aligned} \tag{25}$$

where the square bracket in Hermite coefficient denotes permutations (*e.g.*, $[\boldsymbol{F}\mathbf{uu}] = \boldsymbol{F}\mathbf{uu} + \mathbf{u}\boldsymbol{F}\mathbf{u} + \mathbf{uu}\boldsymbol{F}$), and $\hat{\boldsymbol{\mathcal{H}}}$ is obtained by replacing $\boldsymbol{c}_i$ by $\boldsymbol{c}_i/c_s$ and c_s^2 by 1 in Eqs.(24). Eventually, we obtain the following post-collision central moments:

$$\begin{aligned}k_0^\star &= \tilde{p},\\ k_1^\star &= (1-\tilde{p})\,u_x + F_x/(2\rho),\\ k_2^\star &= (1-\tilde{p})\,u_y + F_y/(2\rho),\\ k_3^\star &= \tilde{p}\left(u_x^2 + u_y^2 + 2c_s^2\right) - u_x^2 - u_y^2,\\ k_4^\star &= (1-\omega)\,k_4 + \omega\,(\tilde{p}-1)\left(u_x^2 - u_y^2\right),\\ k_5^\star &= (1-\omega)\,k_5 + \omega\,(\tilde{p}-1)\,u_xu_y,\\ k_6^\star &= (1-\tilde{p})\left(u_x^2 + c_s^2\right)u_y + F_yc_s^2/(2\rho),\\ k_7^\star &= (1-\tilde{p})\left(u_y^2 + c_s^2\right)u_x + F_xc_s^2/(2\rho),\\ k_8^\star &= \tilde{p}\left[c_s^2 + c_s^4\left(u_x^2 + u_y^2\right) + u_x^2u_y^2\right]\\ &\quad - c_s^2\left(u_x^2 + u_y^2\right) - u_x^2u_y^2.\end{aligned} \tag{26}$$

where

$$k_4 = \sum_i f_i\left(\bar{c}_{ix}^2 - \bar{c}_{iy}^2\right), \quad k_5 = \sum_i f_i\bar{c}_{ix}\bar{c}_{iy}. \tag{27}$$

Notice that present post-collision CMS degrade exactly into those obtained in De Rosis & Luo (2019) for one-component flows when $p = \rho c_s^2$. Then, post-collision populations are reconstructed as $|f_i^\star\rangle = \mathbf{T}^{-1}\,|k_i^\star\rangle$, that are eventually streamed by Eq. (3).

We now rewrite the LBE in a general multiple-relaxation-time (GMRT) framework (Fei & Luo (2017); Fei, Luo, & Li (2018)). Indeed, the matrix $\mathbf{T}$ can be written as the product of two contribution, $\mathbf{T} = \mathbf{NM}$. Hence, post-collision populations can be rewritten as

$$|f_i^\star\rangle = \mathbf{T}^{-1}\,|k_i^\star\rangle = \mathbf{M}^{-1}\mathbf{N}^{-1}\,|k_i^\star\rangle\,, \tag{28}$$

where the transformation matrix $\mathbf{M}$ transforms the distribution functions into raw moments and is obtained by replacing $\bar{c}_i$ with c_i in Eq. (21).The shift matrix (originally introduced in Asinari (2008)) is $\mathbf{N} = \mathbf{T}\mathbf{M}^{-1}$ and transforms raw moments into central moments. If this shift is neglected, i.e., $\mathbf{N} = \mathbf{I}$, then $\mathbf{T} = \mathbf{M}$. In other words, the classical (raw-moments-based) multiple-relaxation-time can be viewed as a particular case of a general (central-moments-based) multiple-relaxation-time LBM. In practical terms, we first compute post-collision raw moments $|r_i^\star\rangle$ as $|r_i^\star\rangle = \mathbf{N}^{-1}\,|k_i^\star\rangle$, and then we transform into populations as $|f_i^\star\rangle = \mathbf{M}^{-1}\,|r_i^\star\rangle$.

2.3.2 | CMs-based LBM for g_i

Very interestingly, the same algorithmic procedure above described for f_i can be adopted to derive a CMs-based formulation for the other set of populations, g_i. In this case, the post-collision populations are

$$|g_i^\star(\boldsymbol{x},t)\rangle = |g_i(\boldsymbol{x},t)\rangle + \boldsymbol{\Lambda}_\phi[|g_i^{\mathrm{eq}}(\boldsymbol{x},t)\rangle - |g_i(\boldsymbol{x},t)\rangle] + (\mathbf{I}-\boldsymbol{\Lambda}_\phi/2)\,|G_i(\boldsymbol{x},t)\rangle\,. \tag{29}$$

Similarly to the approach adopted for f_i, the equilibrium distributions can be projected into a basis of Hermite polynomials $\boldsymbol{\mathcal{H}}^{(n)}$ as

$$g_i^{\mathrm{eq}} = w_i\phi\left[1+\frac{\boldsymbol{c}_i\cdot\mathbf{u}}{c_s^2}+\frac{1}{2c_s^4}\boldsymbol{\mathcal{H}}_i^{(2)}:\mathbf{uu} + \frac{1}{2c_s^6}\left(\boldsymbol{\mathcal{H}}^{(3)}_{ixxy}u_x^2u_y+\boldsymbol{\mathcal{H}}^{(3)}_{ixyy}u_xu_y^2\right)+\frac{1}{4c_s^8}\boldsymbol{\mathcal{H}}^{(4)}_{ixxyy}u_x^2u_y^2\right], \tag{30}$$

that recovers Eq. (8) when $\boldsymbol{\mathcal{H}}^{(3)}$ and $\boldsymbol{\mathcal{H}}^{(4)}$ are disregarded. By using the very same shifting matrix (see Eq. (21)), the collision matrix can be written as $\boldsymbol{\Lambda}_\phi = \mathbf{T}^{-1}\mathbf{K}_\phi\mathbf{T}$, where $\mathbf{K}_\phi = \mathrm{diag}[1, \omega_\phi, \omega_\phi, 1, 1, 1, 1, 1, 1]$ is the corresponding relaxation matrix, with $\omega_\phi = 1/(\tau_\phi + 1/2)$. By collecting pre-collision, equilibrium and post-collision CMs as $|k_{i,\phi}\rangle = \mathbf{T}\,|g_i\rangle$, $|k_{i,\phi}^{\mathrm{eq}}\rangle = \mathbf{T}\,|g_i^{\mathrm{eq}}\rangle$, and $|k_{i,\phi}^\star\rangle$, respectively, the latter can be written as

$$|k_{i,\phi}^\star\rangle = (\mathbf{I}-\mathbf{K}_\phi)\,|k_{i,\phi}\rangle + \mathbf{K}_\phi\,|k_{i,\phi}^{\mathrm{eq}}\rangle + \left(\mathbf{I}-\frac{\mathbf{K}_\phi}{2}\right)|R_{i,\phi}\rangle\,. \tag{31}$$

Again, we need to compute the central moments of the discrete forcing term. Analogously to what we have done for F_i, here we propose to adopt the full set of Hermite polynomials, leading to

$$G_i = w_i\left(\frac{\boldsymbol{F}_\phi}{c_s}\cdot\hat{\boldsymbol{\mathcal{H}}}^{(1)}+\frac{[\boldsymbol{F}_\phi\mathbf{u}]}{2c_s^2}\cdot\hat{\boldsymbol{\mathcal{H}}}^{(2)} + \frac{[\boldsymbol{F}_\phi\mathbf{uu}]}{6c_s^3}\cdot\hat{\boldsymbol{\mathcal{H}}}^{(3)}_{[xyy],[xxy]}+\frac{[\boldsymbol{F}_\phi\mathbf{uuu}]}{24c_s^4}\cdot\hat{\boldsymbol{\mathcal{H}}}^{(4)}_{[xxyy]}\right). \tag{32}$$

The CMs of the present discrete force term can be computed as $|R_{i,\phi}\rangle = \mathbf{T}\,|G_i\rangle$ and read as $R_{1,\phi} = F_{x,\phi}$, $R_{2,\phi} = F_{y,\phi}$, $R_{6,\phi} = F_{y,\phi}c_s^2$, $R_{7,\phi} = F_{x,\phi}c_s^2$, with $R_{0,\phi} = R_{3,\phi} = R_{4,\phi} = R_{5,\phi} = R_{8,\phi} = 0$. Post-collision CMs are:

$$\begin{aligned}
k_{0,\phi}^\star &= \phi,\\
k_{1,\phi}^\star &= (1-\omega_\phi)\,k_{1,\phi} + F_{x,\phi}/2,\\
k_{2,\phi}^\star &= (1-\omega_\phi)\,k_{2,\phi} + F_{y,\phi}/2,\\
k_{3,\phi}^\star &= 2\phi c_s^2,\\
k_{6,\phi}^\star &= F_{y,\phi}c_s^2/2,\\
k_{7,\phi}^\star &= F_{x,\phi}c_s^2/2,\\
k_{8,\phi}^\star &= \phi c_s^4,
\end{aligned} \tag{33}$$

where

$$k_{1,\phi} = \sum_i g_i\bar{c}_{ix}, \qquad k_{2,\phi} = \sum_i g_i\bar{c}_{iy}. \tag{34}$$

Before being streamed by Eq. (4), the post-collision populations are reconstructed as

$$|g_i^\star\rangle = \mathbf{T}^{-1}\,|k_{i,\phi}^\star\rangle = \mathbf{M}^{-1}\mathbf{N}^{-1}\,|k_{i,\phi}^\star\rangle\,. \tag{35}$$

By using the very same arguments as those explained for f_i, the LBE governing the evolution of g_i can be rewritten in the GMRT framework. Indeed, the two sets of populations share not only the same space-and-time discretization, but the same discrete velocity representation too (i.e., the D2Q9 model). Consistently, the matrices $\mathbf{T}$, $\mathbf{M}$ and $\mathbf{N}$ remain unchanged. Once again, we can assess that the classical raw-moments-based multiple-relaxation-time LBM can be obtained as a particular case of the present methodology that is obtained when $\mathbf{N} = \mathbf{I}$. To adopt the "two-step" reconstruction (Fei & Luo (2017)), we can compute post-collision raw moments $|r_{i,\phi}^\star\rangle$ as $|r_{i,\phi}^\star\rangle = \mathbf{N}^{-1}\,|k_{i,\phi}^\star\rangle$, and then we transform into populations as $|g_i^\star\rangle = \mathbf{M}^{-1}\,|r_{i,\phi}^\star\rangle$.

It should be noted that boundary conditions for the phase field can be applied similarly to the ones for the flow field. For example, the presence of a straight wall at a certain location $\boldsymbol{x}'$ obeys the bounce-back rule and reads as follows:

$$f_i(\boldsymbol{x}',t) = f_{i^\dagger}^\star(\boldsymbol{x}',t), \qquad g_i(\boldsymbol{x}',t) = g_{i^\dagger}^\star(\boldsymbol{x}',t), \tag{36}$$

where $i^\dagger$ is the lattice direction opposite to i.

2.3.3 | Algorithm of computation

For an easy reproducibility of the results presented in the next section and to fully understand the algorithmic procedure, herein we report the actions to be taken within the typical time step according to the proposed scheme.

- Compute the macroscopic variables:

$$\tilde{p} = \sum_i f_i, \quad \mathbf{u} = \sum_i f_i\mathbf{c}_i, \quad \phi = \sum_i g_i, \qquad \rho = \rho_L + \frac{\phi-\phi_L}{\phi_H-\phi_L}(\rho_H-\rho_L)\,. \tag{37}$$

- Evaluate the spatial derivatives of the order parameter by Eqs. (15), as well as those of the velocity ($\boldsymbol{\nabla}\mathbf{u}$) and density ($\boldsymbol{\nabla}\rho$).

- Calculate $\nu = \tau c_s^2$ by interpolating τ as

$$\tau = \tau_L + \frac{\phi - \phi_L}{\phi_H - \phi_L}\left(\tau_H - \tau_L\right). \tag{38}$$

- Obtain the forces $\boldsymbol{F} = \boldsymbol{F}_s + \boldsymbol{F}_p + \boldsymbol{F}_\mu + \boldsymbol{F}_b$, where

$$\boldsymbol{F}_s = \mu_\phi \boldsymbol{\nabla}\phi,\ \boldsymbol{F}_p = -\tilde{p}c_s^2\boldsymbol{\nabla}\rho,\ \boldsymbol{F}_\mu = \nu\left[\boldsymbol{\nabla}\mathbf{u} + (\boldsymbol{\nabla}\mathbf{u})^\top\right]\cdot\boldsymbol{\nabla}\rho, \tag{39}$$

  where μ_ϕ is the chemical potential in Eq.(14) and $\boldsymbol{F}_b$ accounts for gravity and immersed boundary forces (see De Rosis, Ubertini, & Ubertini (2014)).

- Correct the fluid velocity:

$$\mathbf{u} = \sum_i f_i \mathbf{c}_i + \frac{\boldsymbol{F}}{2} \tag{40}$$

- Determine the vector $\boldsymbol{F}_\phi$:

$$\boldsymbol{F}_\phi = c_s^2 \frac{1 - 4\left(\phi - \phi_0\right)^2}{\xi}\cdot\frac{\boldsymbol{\nabla}\phi}{|\boldsymbol{\nabla}\phi|}. \tag{41}$$

- Compute the only non-zero pre-collision central moments:

$$\begin{aligned} k_4 &= \sum_i f_i\left(\bar{c}_{ix}^2 - \bar{c}_{iy}^2\right), \quad k_5 = \sum_i f_i \bar{c}_{ix}\bar{c}_{iy}, \\ k_{1,\phi} &= \sum_i g_i \bar{c}_{ix}, \qquad\qquad k_{2,\phi} = \sum_i g_i \bar{c}_{iy}. \end{aligned} \tag{42}$$

- Calculate the post-collision ones $|k_i^\star\rangle$ and $|k_{i,\phi}^\star\rangle$ as in Eqs.(26) and Eqs.(33), respectively. Notice that these depend on previously computed quantities: $\tilde{p}$, $\boldsymbol{u}$, ϕ, $\boldsymbol{F}$ and $\boldsymbol{F}_\phi$, as well as on the relaxation frequencies $\omega = 1/(\tau + 1/2)$ and $\omega_\phi = 1/(\tau_\phi + 1/2)$.

- Reconstruct post-collision populations for the flow and phase fields, respectively:

$$|f_i^\star\rangle = \mathbf{M}^{-1}\mathbf{N}^{-1}\,|k_i^\star\rangle\,,\ |g_i^\star\rangle = \mathbf{M}^{-1}\mathbf{N}^{-1}\,|k_{i,\phi}^\star\rangle\,, \tag{43}$$

- Stream both the sets of populations as

$$\begin{aligned} |f_i(\boldsymbol{x} + \boldsymbol{c}_i, t+1)\rangle &= |f_i^\star(\boldsymbol{x}, t)\rangle\,, \\ |g_i(\boldsymbol{x} + \boldsymbol{c}_i, t+1)\rangle &= |g_i^\star(\boldsymbol{x}, t)\rangle\,, \end{aligned} \tag{44}$$

  and advance in time.

Furthermore, the script D2Q9CentralMomentsPhaseField.m is attached as Supplementary Material. It allows the reader to perform all the involved symbolic manipulations in order to re-build our proposed model.

3 | NUMERICAL EXPERIMENTS

The results of our numerical investigation are presented herein. Specifically, the numerical performance of the novel LB methodology outlined in Section 2.3 is elucidated against four benchmark problems: a stability analysis for a partially submerged cube in an unstable equilibrium after an initial perturbation is imposed (Campbell & Vignjevic (2012); Fekken (2004)); the free fall of a cylinder in quiescent water (Colicchio, Greco, Miozzi, & Lugni (2009)); the rise of a submerged cylinder in quiescent water (Campbell & Vignjevic (2012); Fekken (2004)); and the vertical penetration of a wedge (Wagner (1932)). In all the computations, we consider a system composed of two immiscible fluids: the heavy one, water, with $\rho_H = 1000\,\mathrm{kg/m^3}$ and $\nu_H = 10^{-6}\,\mathrm{m^2/s}$, and the light one, air, with $\rho_L = 1.225\,\mathrm{kg/m^3}$ and $\nu_L = 1.5 \times 10^{-5}\,\mathrm{m^2/s}$. At the beginning of each run, the two fluids are at rest, i.e. $\mathbf{u}_{L,H}(t=0) = 0$. A gravitational acceleration equal to $a = 9.81\,\mathrm{m/s^2}$ is used. In addition, we set $M = 0.1$ and $\xi = 4$. These values stem from preliminary analyses, where M and ξ have been varied in a wide range and then selected in order to obtain an optimal balance between stable and accurate runs. Moreover, we choose $\sigma = 1 \times 10^{-5}$. Unless otherwise stated, the leading dimension of the submerged rigid body is idealized by 100 points. Computations performed in this research are in dimensionless lattice units, where the time step and grid spacing are both equal to 1. In order to simulate a real-life scenario, a conversion of units must be carried out previously. An example is given in Appendix B.

When a moving solid body is considered, its presence is accounted for by the Immersed Boundary method (Feng & Michaelides (2009); Mittal & Iaccarino (2005); Peskin (2002)). In short, the solid surface is represented by a set of nodes that can freely move on the underlying lattice grid. The no-slip condition at the fluid-structure interface is enforced by interpolation/extrapolation rules, generating a body force term that is accounted for in Eq. (12) (De Rosis et al. (2014)). Here, we restrict our analyzes to squared and cylindrical solids. However, the generality of the adopted Immersed Boundary method allows us to compute fluid forces acting upon any arbitrarily shaped bodies. Our tests involve rigid moving bodies whose dynamics is evaluated by a second-order accurate Adam-Bashfort scheme (Butcher & Goodwin (2008)). Vectors collecting the displacements and velocities of the center of mass of the rigid body are denoted as $\mathbf{q} = [q_x, q_y]$ and $\dot{\mathbf{q}} = [\dot{q}_x, \dot{q}_y]$, respectively, where the superimposed dot indicates the time derivative, i.e., $\dot{\mathbf{q}} = \dfrac{\partial \mathbf{q}}{\partial t}$.

Finally, the SPH solver DualSPHysics (Crespo et al. (2015)) is used for validation purposes. Simulations are run using a Weakly-Compressible SPH (WCSPH) formulation where the Euler equations are stabilized by an artificial viscosity, also

acting as an effective fluid bulk viscosity. Boundary conditions for the solid objects are enforced through SPH particles and ghost nodes mirrored into the fluids, following a procedure similar to the one in Marrone, Colagrossi, Antuono, Colicchio, & Graziani (2013) and Tafuni, Domínguez, Vacondio, & Crespo (2018). Other relevant simulation parameters are kept constant throughout the different cases unless otherwise noted, and are a smoothing-length-to-particle-spacing ratio of 1.5, a speed of sound equal to 20 times the characteristic flow speed, and the use of density diffusion to smooth the pressure field.

3.1 | Pitch decay of a partially submerged object in an initially unstable equilibrium

As shown in FIGURE 1 , our first application of the model involves a cube with sides of length $L = 0.1\,\mathrm{m}$ is submerged in water for half of its volume. A perturbation in the form

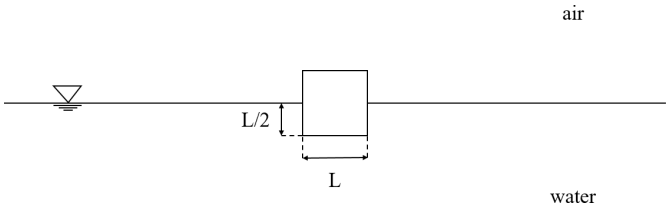

FIGURE 1 Pitch decay of a partially submerged object: sketch of the problem setup.

of an initial angular velocity is applied to the cube. Due to such perturbation, the initial, unstable equilibrium is lost because the submerged portion of the cube volume changes over time, causing the cube to pitch back and forth until a new, stable equilibrium is achieved. The case configuration followed herein is the same as in Fekken (2004) to allow for a direct comparison of the numerical results. However, results in Fekken (2004) were obtained by the volume-of-fluid method. Our computational domain is composed of 500×500 lattice points.

In FIGURE 2 , the time history of the rotation angle obtained by the present LB scheme is compared to findings from a SPH simulation, showing a very good match. Moreover, these two solutions show an oscillatory transient behavior strikingly similar to the one in Fekken (2004), with oscillations characterized by slightly lower amplitudes. Notably, the theoretical values of 45 degrees is successfully captured.

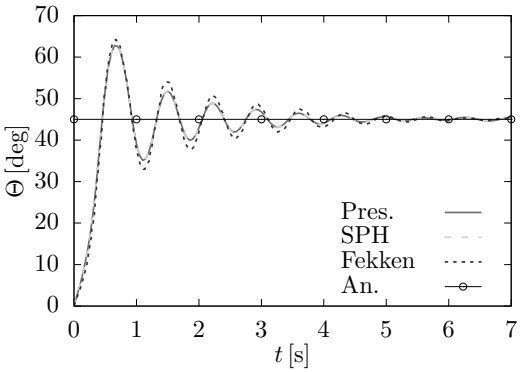

FIGURE 2 Time history of the angle of rotation for the pitch decay simulation. Numerical solutions generated by the proposed LBM (solid line), SPH (dashed line) and CFD study in Fekken (2004) (dotted line) are compared to the analytical prediction of 45 degrees (straight line with circles).

3.2 | Impact of a free falling cylinder on a quiescent viscous liquid

Next, the free fall of a cylinder as described in Colicchio et al. (2009) is analyzed. The sketch of this test case is presented in FIGURE 3 . A cylinder with a diameter $D = 0.3\,\mathrm{m}$ impacts a body of quiescent water at a velocity of $v_i = 2.55\,\mathrm{m/s}$. The domain is composed of 8000 and 3200 points in the

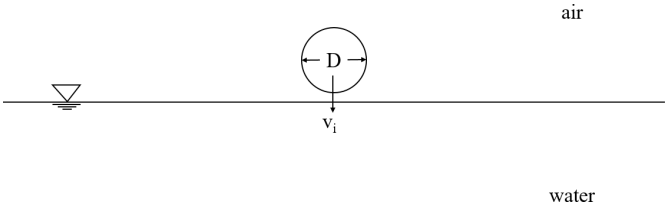

FIGURE 3 Falling cylinder: sketch of the problem setup.

horizontal and vertical directions, respectively. The diameter of the cylinder is represented by 400 points. LB results are reported in FIGURE 4 in terms of vertical component of the cylinder velocity and displacement of the cylinder's center of mass, and compared to experimental and numerical findings by the level set method in Colicchio et al. (2009) and SPH simulations, respectively.

The new LB model predicts the entry phase (up to $t = 0.4\,\mathrm{s}$) very well. Interestingly, the computed negative peak in the curve showing the position of the cylinder's center of mass overlaps the two other numerical results to a great extent. A discrepancy is more noticeable when the cylinder moves back upward: in this phase, the proposed LBM approach exhibits a very similar peak value as the other techniques, but with a

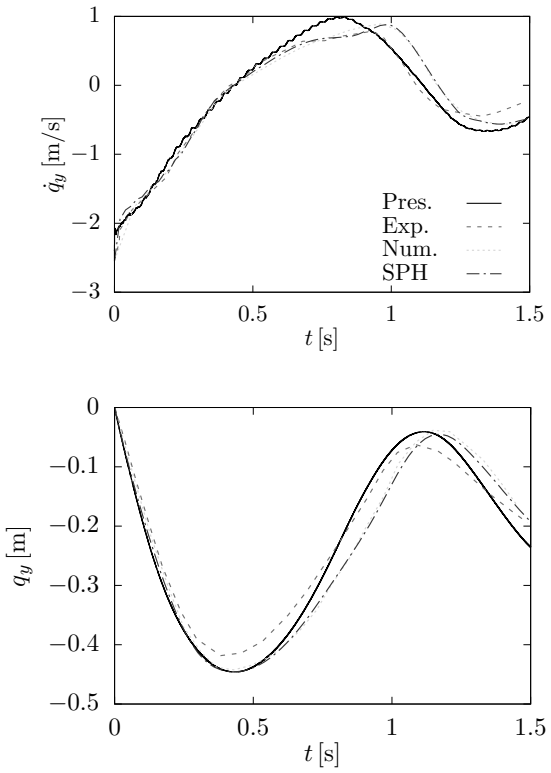

FIGURE 4 Free falling cylinder: time evolution of the vertical component of the velocity (top) and displacement of the center of mass of the cylinder (bottom). Present LB scheme (Pres., solid line), experimental (Exp., dashed line) and numerical results (Num., dotted line) in Colicchio et al. (2009) and SPH predictions (dash-dotted line).

	Pres.	Exp.	Num.	SPH
$\max(\dot{q}_y)$	0.9955	0.8912	0.7868	0.8798
$-\min(q_y)$	0.4459	0.4423	0.4185	0.4455

TABLE 1 Free falling cylinder: peak values of $\dot{q}_y$ and q_y obtained by the present approach (Pres.), experimental (Exp.) and numerical (Num.) findings in Colicchio et al. (2009) and SPH run.

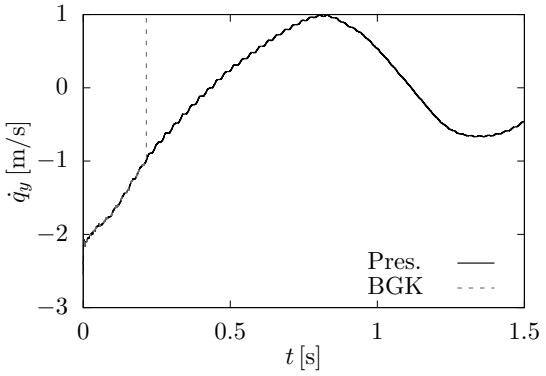

FIGURE 5 Free falling cylinder: time evolution of the vertical component of the velocity by different LB approaches: present CMS-based LBM (solid line) and BGK LBM (dashed line). The latter generates a simulation that blows up at $t \sim 0.2$ s.

slight anticipation in time. This behavior is attributed to the discretization of the interface between the two fluids, currently characterized by a finite thickness of four grid points (i.e., $\xi = 4$), while it should ideally be zero. This is a common issue in the so-called diffuse interface methods. Indeed, the value of ξ has been chosen through preliminary analyses to obtain an optimal balance between stability and accuracy. For the sake of completeness, an additional simulation has been performed by halving the grid spacing, but the value of the discrepancy still persists. Further refinements of the adopted grid can be carried out at the price of an increased computational cost (see Appendix A). A more quantitative estimation is provided in TABLE 1 , where the peak values of $\dot{q}_y$ and q_y are synthetically reported.

This test case is used to demonstrate the superior properties of the CMs-based approach. Specifically, the LB run is repeated by adopting the existing BGK LBM (see Section 2.2). In FIGURE 5 , the time evolution of the vertical component of the velocity is presented by adopting the two LB schemes. This comparison shows the superior stability properties of the present novel methodology. The BGK run blows up at $t \sim 0.2$ s, while the present CMs-based experiment is able to simulate the entire time span. Therefore, we conclude that the adoption of central moments is instrumental to perform more stable simulations and to investigate a water-entry problem as the one considered here.

FIGURE 6 sketches the evolution of the water domain at different time instants for our new LB model (top octuple) and SPH (bottom octuple). For LB results, it can be seen that the impact of the cylinder induces a symmetric deformation of the interface. The cylinder penetrates the water until $t = 0.4$ s. Then, the buoyancy force overcomes the weight and the cylinder starts moving upward. It can be noticed how the cylindrical body is perfectly impermeable, thus underlining the ability of our novel LB scheme to enforce the no-slip condition around a solid body in an excellent way. When comparing the LB contours with the SPH contours in FIGURE 6 , it can be inferred that the two solutions agree to a good extent. Although SPH delivers more details of the splashdown and subsequent jet resurge thanks to its particle description, it can be seen how the two methods agree on the overall time history of free-surface deformation and cylinder position. Specifically,

(a) LBM

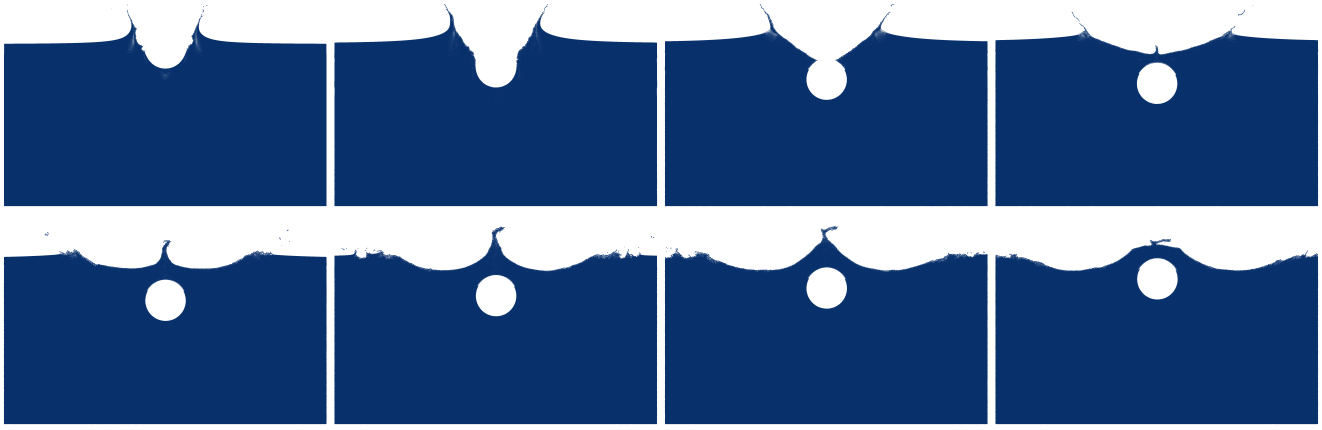

(b) SPH

FIGURE 6 Free falling cylinder: evolution of the water domain at different time instants for LBM and SPH simulations. Considering one octuple, from left to right of the top panel: $t = 0.1, 0.2, 0.3, 0.4$ s; from left to right of the bottom panel: $t = 0.5, 0.6, 0.7, 0.8$ s.

both methods predict a penetration up to $t = 0.4$ s and a subsequent rise of the cylinder due to the buoyant force overtaking weight and the residual kinetic energy. The two methods also agree on the ventilation and subsequent wetting of the upper portion of the cylinder as it penetrates the water. Overall, a good agreement is found. However, the SPH is more capable of capturing the finest flow features, especially near the interface. The discrepancies between the two solutions should be addressed to how our LB method discretizes the free surface, i.e. through a finite thickness, and also to the substantially different nature of the two methods. In fact, the Eulerian nature of the LBM admits smoother deformations of the water-air interface, while the Lagrangian essence of the SPH allows us to better capture violent and rapid changes in the configuration of the free surface.

3.3 | Rising cylinder in a quiescent viscous liquid

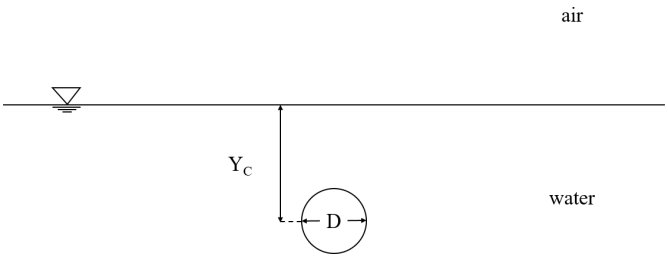

FIGURE 7 Rising cylinder: sketch of the problem setup.

This next case focuses on the rise of a fully submerged cylinder to the free surface. The schematics of this simulation

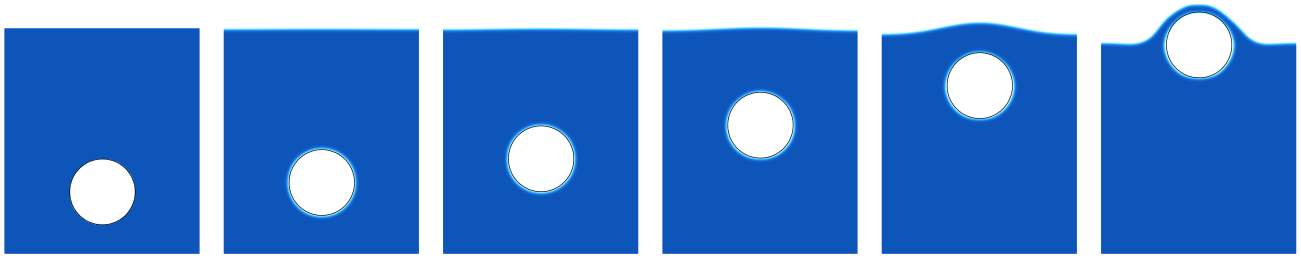

(a) LBM

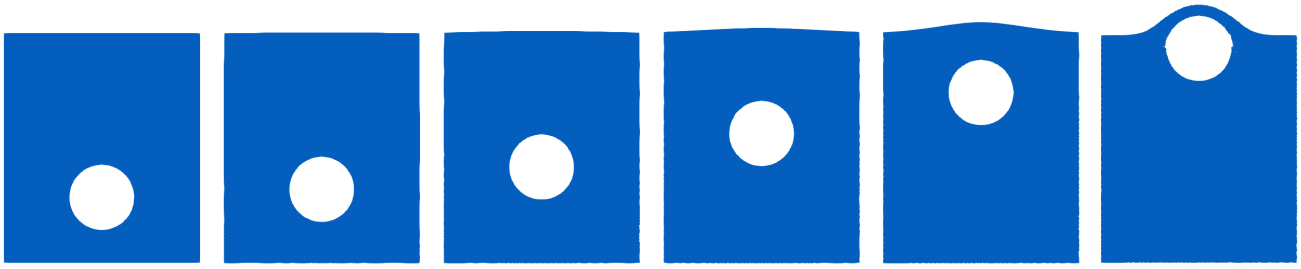

(b) SPH

FIGURE 8 Rising cylinder in a quiescent liquid: evolution of the water domain at different time instants for LBM and SPH solutions. Considering one sixuple, from left to right: $t = 0$, 0.5, 1.0, 1.5, 2.0, and 2.5 s.

are shown in FIGURE 7 , where the submergence depth Y_C is calculated from the resting free surface to the geometric center of the cylinder. For this test case, the conditions in Fekken (2004) and Campbell & Vignjevic (2012) are considered for an easy comparison of the results. The cylinder has a diameter $D = 2\,\text{m}$, a density equal to 0.6 times that of water and its center of mass initially at a depth of 5 m from the water-air interface, i.e. $Y_C = 2.5D$. The fluid domain has a width of $3D$ and an initial water depth equal to $3.5D$. 300 and 500 lattices are adopted in the horizontal and vertical directions, respectively.

FIGURE 8 sketches the evolution of the water domain at different time instants. Similarly to previous cases, a symmetric deformation of the interface between the two fluids and a perfect impenetrability of the solid surface can be appreciated. LB results in FIGURE 8 (top panel) show a very good agreement with those obtained with SPH (bottom panel) with the same level of resolution, i.e. setting the particle spacing in SPH to match the grid size in LB. The position of the cylinder as predicted by the two methods in all time snapshots is almost identical. Furthermore, the free surface deformation which becomes more visible at times $t \geq 1.5$ s is also strikingly similar, highlighting the capability of the new LB approach to tackle this problem.

In FIGURE 9 , the vertical component of the velocity ($\dot{q}_y$) and displacement of the center of mass (q_y) of the cylinder are reported. From a standpoint of flow velocity, these results highlight a very good agreement with data in Fekken (2004)

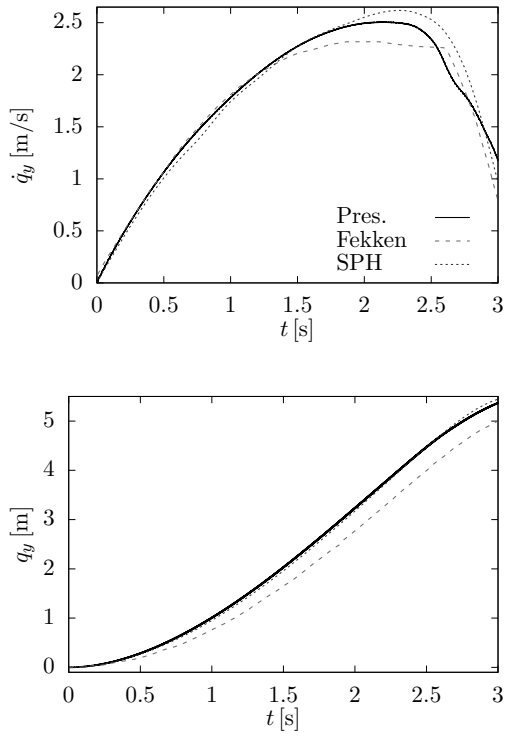

FIGURE 9 Rising cylinder: time evolution of the vertical component of the velocity and displacement of the center of mass of the cylinder by different approaches: present scheme (solid line), findings in Fekken (2004) (dashed line) and SPH simulation (dotted line).

until $t \sim 1.2$ s. Moreover, LB findings are also considerably close to results obtained via SPH in the same time range. For times larger than 1.2 s, our approach overestimates $\dot{q}_y$ when the cylinder crosses the interface. Again, we address this behavior to the width of the interface between the two fluids in the LB approach. Then, the gravitational force dominates the cylinder dynamics, with the proposed scheme able to simulate the downward motion similarly to data in Fekken (2004). Interestingly, a very close agreement is found between the LB and SPH solutions in terms of vertical displacement. For a more quantitative comparison, TABLE 2 reports the peak values of $\dot{q}_y$ and q_y by the different approaches.

	Pres.	Num.	SPH
max $(\dot{q}_y)$	2.5079	2.3165	2.6184
max (q_y)	5.4700	5.2368	5.5396

TABLE 2 Rising cylinder: peak values of $\dot{q}_y$ and q_y obtained by the present approach (Pres.), numerical findings in Fekken (2004) (Num.) and SPH run.

3.4 | Vertical penetration of a wedge

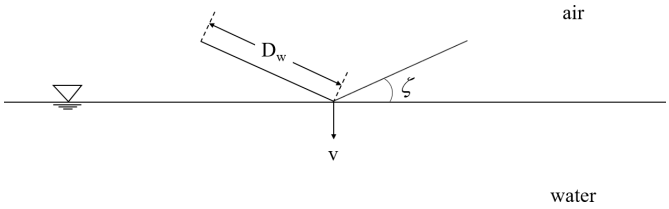

FIGURE 10 Vertical penetration of a wedge: sketch of the problem setup.

As sketched in FIGURE 10 , a symmetric wedge-shaped body with deadrise angle ζ impacting the free surface is simulated next. The length of the semi-wedge is $D_w = 1$ m and it is represented by 500 grid points. 2000 and 1000 lattice points are employed in the horizontal and vertical directions, respectively. A constant uniform downward velocity equal to $v = 1$ m/s is assigned. We compute the resultant of the pressures acting upon the semi-wedge, P, and we compare our findings to the analytical predictions by Wagner (1932)

$$F_W(t) = \rho_H \frac{\pi^2 v^2 a_W(t)}{4 \tan\zeta}, \tag{45}$$

where $a_W(t) = \pi v t/(2\tan\zeta)$ is Wagner's wetted length. Wagner's theory is built on the assumptions of incompressible irrotational flow and inviscid fluid. Gravity and air trapping are also neglected. In addition, it accounts for the motion of the free surface by increasing the value of the wetted length corresponding to a flat surface by a factor $\pi/2$, that is $vt/(\tan\zeta)$ (see Von Karman (1929)). The deadrise angle varies as $\zeta = 2°, 3°, 4°$ in our simulations.

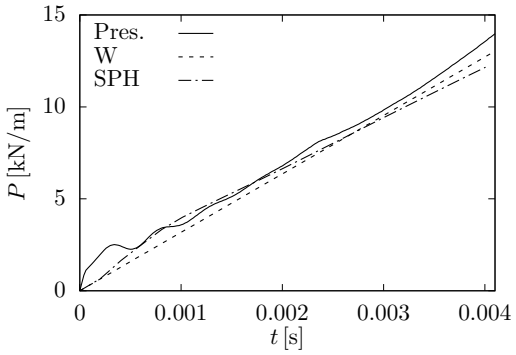

(a) $\zeta = 2°$.

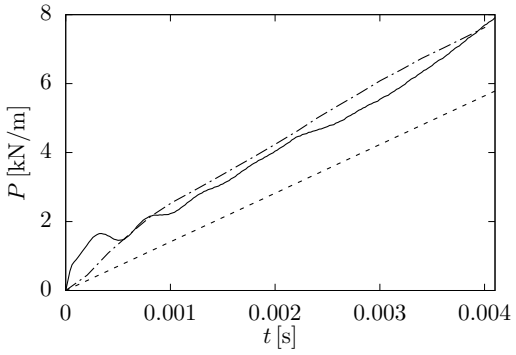

(b) $\zeta = 3°$.

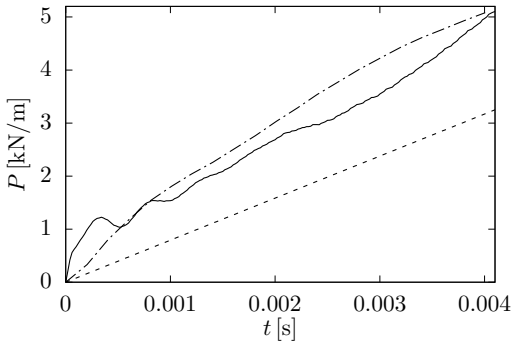

(c) $\zeta = 4°$.

FIGURE 11 Vertical penetration of a wedge: time evolution of the pressure force acting upon the semi-wedge computed by the present approach (Pres. – solid line), Wagner's equation (W – dashed line) for different deadrise angles and SPH simulations (SPH – dash-dotted line).

FIGURE 11 depicts the time evolution of the LB pressure resultant (obtained by integrating over the semi-wedge's length), P, and the same quantity predicted by Wagner (1932), F_{W}, together with findings from SPH simulations. One can immediately appreciate that the results obtained by the two numerical approaches are in very good agreement, hence demonstrating the ability of our method to simulate this problem. After some initial oscillations due to the transient dynamics of the very beginning of the simulations, a linear dependence of P on t is found in the LB runs, consistently with the theoretical predictions in Eq. (45). Moreover, analytical forces decrease as the deadrise angle ζ increases and this is also captured by the proposed approach. It should also be noted that Wagner's theory is valid for very small deadrise angle. Hence, one expects that our numerical findings diverge from the analytical ones as ζ grows. Defining the slope of the $P-t$ diagram as S_{Pres}, taken as the difference between the force at $t = 0.004\,\mathrm{s}$ and the one at $t = 0.002\,\mathrm{s}$ divided by the corresponding time interval, we obtain

$$S_{\mathrm{Pres}} = \frac{P(t = 0.004\,\mathrm{s}) - P(t = 0.002\,\mathrm{s})}{0.004\,\mathrm{s} - 0.002\,\mathrm{s}}. \tag{46}$$

Analogously, S_{W} is defined as the slope of the $F_{\mathrm{W}} - t$ curve, that is

$$S_{\mathrm{W}} = \frac{F_{\mathrm{W}}(t = 0.004\,\mathrm{s}) - F_{\mathrm{W}}(t = 0.002\,\mathrm{s})}{0.004\,\mathrm{s} - 0.002\,\mathrm{s}}, \tag{47}$$

and for the SPH runs

$$S_{\mathrm{SPH}} = \frac{F_{\mathrm{SPH}}(t = 0.004\,\mathrm{s}) - F_{\mathrm{SPH}}(t = 0.002\,\mathrm{s})}{0.004\,\mathrm{s} - 0.002\,\mathrm{s}}. \tag{48}$$

TABLE 3 quantifies the difference of present results with respect to analytical model in terms of relative percent discrepancy between the slopes, i.e.

$$\varepsilon_{\mathrm{W,LB}} = \frac{S_{\mathrm{Pres}} - S_{\mathrm{W}}}{S_{\mathrm{W}}} \times 100. \tag{49}$$

Moreover, we report the relative difference between findings obtained by the SPH runs and the predictions by Wagner as

$$\varepsilon_{\mathrm{W,SPH}} = \frac{S_{\mathrm{SPH}} - S_{\mathrm{W}}}{S_{\mathrm{W}}} \times 100. \tag{50}$$

It is possible to observe that the discrepancy between the numerical solution provided by the present scheme and the analytical solution increases as ζ grows. The SPH exhibits the same trend. Notice that the difference is taken between the slopes, rather than between the values of P itself, due to the fact that the pressure resultant depends linearly on the time (see Eq. (45)). Therefore, even in presence of a very small mismatch between analytical and numerical solutions in the local pressure computation, the discrepancy will be unavoidably much more emphasized as the time advances. Hence, the comparison between the slopes in the $P-t$ diagram represents a more reliable estimation of the accuracy of the method. As an additional tool to investigate the ability of the proposed scheme of reproducing the dynamics of the interface around the wedge, additional runs are carried out by selecting $\zeta = [20°, 25°, 30°, 35°]$. The time evolution of the water domain is plotted in FIGURE 12 for $\zeta = 25°$, where the pile-up along the wedge can be clearly appreciated and further compared to findings in Zarghami et al. (2014). An animation is also available at `https://www.youtube.com/watch?v=lgJ5cndBf6A`.

ζ	2°	3°	4°
$\varepsilon_{\mathrm{W,LB}}$	6.3266	29.4741	44.2311
$\varepsilon_{\mathrm{W,SPH}}$	5.1568	32.2889	46.3319

TABLE 3 Vertical penetration of a wedge: percentage relative discrepancy between (i) the slope of present results and Wagner's predictions, $\varepsilon_{\mathrm{W,LB}}$, and (ii) the slope of SPH findings and Wagner's predictions, $\varepsilon_{\mathrm{W,SPH}}$, for different deadrise angles ζ.

In FIGURE 13 , the air-water interface is depicted at $t = 0.01$ s. Our results show a decrease of the relative water pile-up with increasing deadrise angles. This corroborates findings in Mei, Liu, & Yue (1999), as well as those achieved by a free-surface LB study in Zarghami et al. (2014).

4 | CONCLUSIONS

In this paper, an original phase-field lattice Boltzmann method has been presented and tested against four benchmark problems. The proposed scheme has demonstrated the ability to accurately predict the hydrostatic and hydrodynamic actions in the case of partially and totally submerged objects. In combination with a time integration scheme for solid dynamics, it can be concluded that the present LB scheme is an excellent candidate to perform accurate simulations of realistic hydrodynamic stability and water-entry and water-exit problems. Moreover, the present LB algorithm is competitive with respect to existing strategies in terms of stability of the analysis, especially when high-density contrasts are involved.

The advantages of the proposed approach can be summarized as follows: (i) increased stability with respect to the BGK LBM; (ii) ability to account for high density and viscosity contrasts; (iii) very general formulation, that can be extended to any lattice velocity discretization; (iv) compact practical implementation.

Our next step is the development to a three-dimensional model, that will allow us to simulate more complex and sophisticated problems, as the water-exit of a sphere (Haohao, Yanping, Jianyang, Fu, & Tian (2019)) and the water-entry of hydrophobic objects (Shentu, Zhao, Li, & Zhao (2019)). It

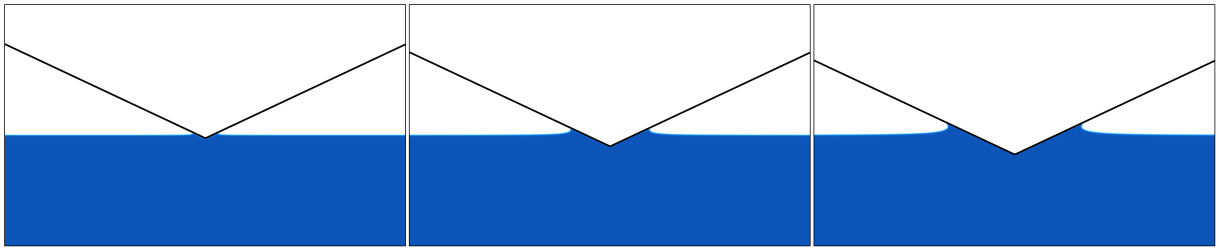

FIGURE 12 Vertical penetration of a wedge: evolution of the water domain for $\zeta = 25°$ at salient time instants, i.e. $t = 0.02$ s (left), 0.06 s (mid), and 0.1 s (right).

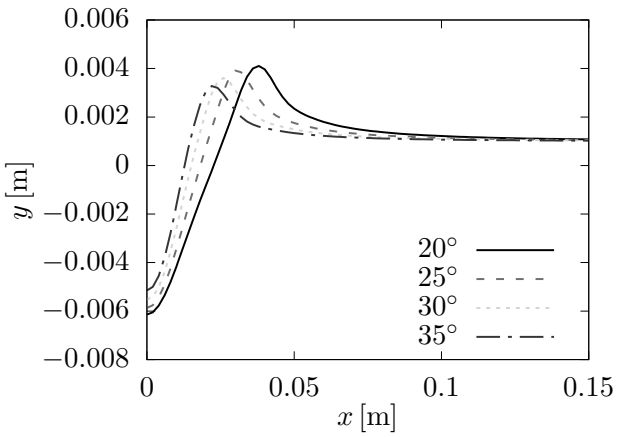

FIGURE 13 Vertical penetration of a wedge: air-water interface at $t = 0.01$ s for different deadrise angle: 20° (solid line), 25° (dashed line), 30° (dotted line) and 35° (dash-dotted line).

should be pointed out that handling more complex geometries, especially in three dimensions, may imply a huge amount of computational time due to the corresponding high number of required lattice points. This issue can be alleviated by using, for example, block-structured grid refinements.

SUPPLEMENTAL MATERIAL

The script D2Q9CentralMomentsPhaseField.m allows the reader to perform all the involved symbolic manipulations in order to re-build our proposed model.

AUTHOR CONTRIBUTIONS

A. De Rosis developed the proposed methodological approach and performed the LBM simulations. A. Tafuni performed all the SPH analyses. Both the authors contributed to writing, editing and formatting the manuscript.

CONFLICT OF INTEREST

The authors declare no potential conflict of interests.

References

Allen, S. M., & Cahn, J. W. (1976). Mechanisms of phase transformations within the miscibility gap of fe-rich fe-al alloys. *Acta Metallica*, *24*(5), 425–437.

Asinari, P. (2008). Generalized local equilibrium in the cascaded lattice Boltzmann method. *Physical Review E*, *78*(1), 016701.

Balendra, T., Wang, C., & Cheong, H. (1995). Effectiveness of tuned liquid column dampers for vibration control of towers. *Engineering Structures*, *17*(9), 668–675.

Bhatnagar, P., Gross, E., & Krook, M. (1954). A model for collision processes in gases. I. small amplitude processes in charged and neutral one-component systems. *Physical Review*, *94*(3), 511.

Butcher, J. C., & Goodwin, N. (2008). *Numerical methods for ordinary differential equations* (Vol. 2). Wiley Online Library.

Campbell, J. C., & Vignjevic, R. (2012). Simulating structural response to water impact. *International Journal of Impact Engineering*, *49*, 1–10.

Chiu, P.-H., & Lin, Y.-T. (2011). A conservative phase field method for solving incompressible two-phase flows. *Journal of Computational Physics*, *230*(1), 185–204.

Colicchio, G., Greco, M., Miozzi, M., & Lugni, C. (2009). Experimental and numerical investigation of the water-entry and water-exit of a circular cylinder. In *24th international workshop on water waves and floating bodies* (pp. 19–22).

Colwell, S., & Basu, B. (2008). Experimental and theoretical investigations of equivalent viscous damping of structures with tlcd for different fluids. *Journal of structural engineering*, *134*(1), 154–163.

Coreixas, C., Wissocq, G., Puigt, G., Boussuge, J.-F., & Sagaut, P. (2017). Recursive regularization step for

high-order lattice boltzmann methods. *Physical Review E*, *96*(3), 033306.

Crespo, A., Altomare, C., Domínguez, J., González-Cao, J., & Gómez-Gesteira, M. (2017). Towards simulating floating offshore oscillating water column converters with smoothed particle hydrodynamics. *Coastal Engineering*, *126*, 11 - 26.

Crespo, A., Domínguez, J., Rogers, B., Gómez-Gesteira, M., Longshaw, S., Canelas, R., … García-Feal, O. (2015). Dualsphysics: Open-source parallel cfd solver based on smoothed particle hydrodynamics (sph). *Computer Physics Communications*, *187*, 204 - 216.

De Rosis, A. (2016). Non-orthogonal central moments relaxing to a discrete equilibrium: A d2q9 lattice boltzmann model. *Europhysics Letters*, *116*, 44003.

De Rosis, A. (2017). Nonorthogonal central-moments-based lattice boltzmann scheme in three dimensions. *Physical Review E*, *95*(1), 013310.

De Rosis, A., Huang, R., & Coreixas, C. (2019). Universal formulation of central-moments-based lattice boltzmann method with external forcing for the simulation of multiphysics phenomena. *Physics of Fluids*, *31*(11), 117102.

De Rosis, A., & Luo, K. H. (2019). Role of higher-order hermite polynomials in the central-moments-based lattice boltzmann framework. *Physical Review E*, *99*(1), 013301.

De Rosis, A., Ubertini, S., & Ubertini, F. (2014). A comparison between the interpolated bounce-back scheme and the immersed boundary method to treat solid boundary conditions for laminar flows in the lattice Boltzmann framework. *Journal of Scientific Computing*, *61*(3), 477-489.

Dinesh Kumar, E., Sannasiraj, S., & Sundar, V. (2019). Phase field lattice boltzmann model for air-water two phase flows. *Physics of Fluids*, *31*(7), 072103.

Domínguez, J. M., Crespo, A. J., Hall, M., Altomare, C., Wu, M., Stratigaki, V., … Gómez-Gesteira, M. (2019). Sph simulation of floating structures with moorings. *Coastal Engineering*, *153*, 103560.

Fakhari, A., Mitchell, T., Leonardi, C., & Bolster, D. (2017). Improved locality of the phase-field lattice-boltzmann model for immiscible fluids at high density ratios. *Physical Review E*, *96*(5), 053301.

Fei, L., & Luo, K. H. (2017). Consistent forcing scheme in the cascaded lattice Boltzmann method. *Physical Review E*, *96*(5), 053307.

Fei, L., Luo, K. H., & Li, Q. (2018, may). Three-dimensional cascaded lattice Boltzmann method: Improved implementation and consistent forcing scheme. *Physical Review E*, *97*(5), 053309.

Fekken, G. (2004). *Numerical simulation of free-surface flow with moving rigid bodies* (Unpublished doctoral dissertation). Rijksuniversiteit Groningen.

Feng, Z.-G., & Michaelides, E. (2009). Robust treatment of no-slip boundary condition and velocity updating for the lattice-Boltzmann simulation of particulate flows. *Computers and Fluids*, *38*(2), 370–381.

Gao, H., Kwok, K., & Samali, B. (1997). Optimization of tuned liquid column dampers. *Engineering structures*, *19*(6), 476–486.

Geier, M., Greiner, A., & Korvink, J. (2006). Cascaded digital lattice Boltzmann automata for high Reynolds number flow. *Physical Review E*, *73*(6), 066705.

Gruszczyński, G., Mitchell, T., Leonardi, C., Laniewski-Wollk, L., & Barber, T. (2019). A cascaded phase-field lattice boltzmann model for the simulation of incompressible, immiscible fluids with high density contrast. *Computers and Mathematics with Applications*.

Haohao, H., Yanping, S., Jianyang, Y., Fu, C., & Tian, L. (2019). Numerical analysis of water exit for a sphere with constant velocity using the lattice boltzmann method. *Applied Ocean Research*, *84*, 163–178.

He, X., & Luo, L.-S. (1997). Theory of the lattice boltzmann method: From the boltzmann equation to the lattice boltzmann equation. *Physical Review E*, *56*(6), 6811.

Huang, R., Wu, H., & Adams, N. A. (2018, may). Eliminating cubic terms in the pseudopotential lattice Boltzmann model for multiphase flow. *Physical Review E*, *97*(5), 053308.

Krüger, T., Kusumaatmaja, H., Kuzmin, A., Shardt, O., Silva, G., & Viggen, E. M. (2017). The lattice boltzmann method. *Springer International Publishing*, *10*(978-3), 4–15.

Kühner, S., Crouse, B., Rank, E., Tölke, J., & Krafczyk, M. (2004). From a product model to visualization: Simulation of indoor flows with lattice-boltzmann methods. *Computer-Aided Civil and Infrastructure Engineering*, *19*(6), 411-420.

Latt, J., & Chopard, B. (2006). Lattice boltzmann method with regularized pre-collision distribution functions. *Mathematics and Computers in Simulations*, *72*(2), 165 - 168.

Leonardi, A., Wittel, F. K., Mendoza, M., Vetter, R., & Herrmann, H. J. (2016). Particle–fluid-structure interaction for debris flow impact on flexible barriers. *Computer-Aided Civil and Infrastructure Engineering*, *31*(5), 323-333.

Malaspinas, O. (2015). Increasing stability and accuracy of the lattice boltzmann scheme: recursivity and regularization. *arXiv preprint arXiv:1505.06900*.

Manjula, E., Ariyaratne, W. H., Ratnayake, C., & Melaaen, M. C. (2017). A review of cfd modelling studies on

pneumatic conveying and challenges in modelling offshore drill cuttings transport. *Powder Technology*, *305*, 782 - 793.

Marrone, S., Colagrossi, A., Antuono, M., Colicchio, G., & Graziani, G. (2013). An accurate SPH modeling of viscous flows around bodies at low and moderate Reynolds numbers. *Journal of Computational Physics*, *245*, 456–475.

Mei, X., Liu, Y., & Yue, D. K. (1999). On the water impact of general two-dimensional sections. *Applied Ocean Research*, *21*(1), 1–15.

Mittal, R., & Iaccarino, G. (2005). Immersed boundary methods. *Annual Review of Fluid Mechanics*, *37*, 239–261.

Mogan, S. C., Chen, D., Hartwig, J., Sahin, I., & Tafuni, A. (2018). Hydrodynamic analysis and optimization of the titan submarine via the sph and finite–volume methods. *Computers & Fluids*, *174*, 271 - 282.

Monaghan, J. J. (1992). Smoothed particle hydrodynamics. *Annual Review of Astronomy and Astrophysics*, *30*(1), 543–574.

Peskin, C. (2002). The immersed boundary method. *Acta Numerca*, *11*(2), 479-517.

Shentu, J., Zhao, T., Li, D., & Zhao, X. (2019). Numerical simulations for water entry of hydrophobic objects. *Ocean Engineering*, *190*, 106485.

Succi, S. (2001). *The lattice Boltzmann equation for fluid dynamics and beyond*. Clarendon.

Tafuni, A., Domínguez, J., Vacondio, R., & Crespo, A. (2018). A versatile algorithm for the treatment of open boundary conditions in smoothed particle hydrodynamics gpu models. *Computer Methods in Applied Mechanics and Engineering*, *342*, 604 - 624.

Tafuni, A., Sahin, I., & Hyman, M. (2016). Numerical investigation of wave elevation and bottom pressure generated by a planing hull in finite-depth water. *Applied Ocean Research*, *58*, 281 - 291.

Velázquez, E. S., & Castillo, P. E. (2008). An adaptive strategy for the local discontinuous galerkin method applied to porous media problems. *Computer-Aided Civil and Infrastructure Engineering*, *23*(4), 238-252.

Von Karman, T. (1929). The impact on seaplane floats during landing.

Wagner, H. (1932). Über stoß-und gleitvorgänge an der oberfläche von flüssigkeiten. *ZAMM-Journal of Applied Mathematics and Mechanics/Zeitschrift für Angewandte Mathematik und Mechanik*, *12*(4), 193–215.

Wang, J., Ni, Y., Ko, J., & Spencer Jr, B. (2005). Magneto-rheological tuned liquid column dampers (mr-tlcds) for vibration mitigation of tall buildings: modelling and analysis of open-loop control. *Computers & structures*, *83*(25-26), 2023–2034.

Zarghami, A., Falcucci, G., Jannelli, E., Succi, S., Porfiri, M., & Ubertini, S. (2014). Lattice boltzmann modeling of water entry problems. *International Journal of Modern Physics C*, *25*(12), 1441012. doi:

Zhu, Z.-w., Gu, M., & Chen, Z.-q. (2007). Wind tunnel and cfd study on identification of flutter derivatives of a long-span self-anchored suspension bridge. *Computer-Aided Civil and Infrastructure Engineering*, *22*(8), 541-554.

How to cite this article: A. De Rosis, A. Tafuni (2020), A phase-field lattice Boltzmann method for the solution of free-surface hydrodynamics problems, *Computer-Aided Civ. Inf.*, 2020;00:1–13.

APPENDIX

A RAW VERSUS CENTRAL MOMENTS

Let us use the Rayleigh-Taylor mechanism to compare the stability of the scheme proposed in this paper to the raw-moments-based multiple-relaxation-time LBM. Let us

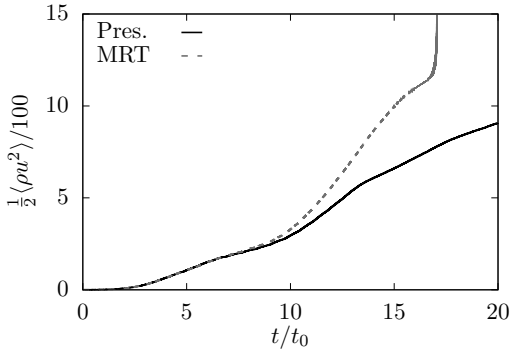

FIGURE A1 Rayleigh-Taylor instability: kinetic energy of the system averaged by the area of the domain obtained by the present scheme (solid line) and raw-moments-based MRT LBM (dashed line). Notice that $\langle\rho u^2\rangle = \frac{1}{N\times 4N}\sum \rho u^2$, with $u^2 = u_x^2 + u_y^2$.

consider a two-dimensional domain of size $N \times 4N$, with $N = 128$, where a fluid of density ρ_H is placed over a lighter one of density $\rho_L = 1$. The fluid is initially at rest and initial conditions in terms of density read as follows

$$\rho(\boldsymbol{x}, 0) = \rho_H, \text{ if } y > 2N + 0.05N\left[\cos\left(2\pi x\right)\right],$$
$$\rho(\boldsymbol{x}, 0) = \rho_L, \text{ otherwise.} \tag{A1}$$

The domain is periodic at every side, except for the top and bottom sections where the no-slip boundary condition is assigned. The flow is driven by a gravitational body force, that is

$$\boldsymbol{F}_b(\boldsymbol{x},t) = -\left[\rho(\boldsymbol{x},t) - \frac{\rho_H+\rho_L}{2}\right]\boldsymbol{a}, \tag{A2}$$

with $\boldsymbol{a} = (0,-a)$, and a chosen so that $\sqrt{aN} = 0.1$. The problem is governed by two dimensionless parameters, that are the Reynolds number $\mathrm{Re} = N\sqrt{gN}/\nu = 3\,000\,000$, and Atwood number, $\mathrm{At} = (\rho_H - \rho_L)/(\rho_H + \rho_L) = 0.1$. FIGURE A1 depicts the kinetic energy of the system averaged by the area of the domain by our approach and by raw-moments-based MRT LBM. While the latter undergoes a blow-up at around $t/t_0 \sim 17.07$ (with $t_0 = \sqrt{N/a}$), the former can successfully simulate a larger time span. Therefore, we can assess that the adoption of central moments is instrumental to perform stable high-Reynolds-number-flow simulations.

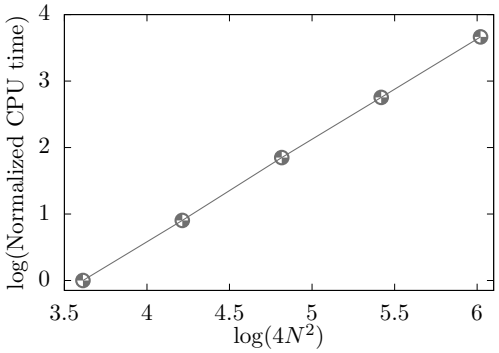

FIGURE A2 Rayleigh-Taylor instability: 10-base logarithm of the requested CPU time against the 10-base logarithm of the number of lattice points $5N$. CPU time is normalized by its value at the coarsest grid resolution, i.e. $N = 32$. The slope of the curve is 1.52.

This test case is further adopted to estimate the computational cost in terms of CPU time involved by our algorithm. Specifically, we run five different simulations by varying N as $N = 32, 64, 128, 256, 512$. In FIGURE A2 , the 10-base logarithm of the requested CPU time (normalized by its value at $N = 32$) is plotted against the 10-base logarithm of the number of lattice points $4N^2$. This graph shows a pretty straight line with slope of 1.52, meaning that the run time of a simulation grows less than quadratically with the number of points. Indeed, particular attention should be paid when progressively higher grid resolutions are involved in the computations.

B UNITS CONVERSION

To perform the conversion from the physical system to the LB world (and vice versa), one should set some scaling factors. Let us consider a cylinder of diameter equal to 1 m. Let us discretize it by (for example) 100 grid points. In this way, it is possible to define the scaling factor for the length as $s_l = \frac{1\,\mathrm{m}}{100} = 0.01\,\mathrm{m}$. Similarly, a physical velocity of $1\,\mathrm{m/s}$ can be represented by a value equal to 0.005 in LB units, thus leading to a velocity scaling factor of $s_v = \frac{1\,\mathrm{m/s}}{0.005} = 200\,\mathrm{m/s}$. Moreover, the scaling factor for the mass density can be set as $s_\rho = 1000\,\mathrm{kg/m^3}$. Given this three values, the remaining conversion parameters can be easily computed. For example, the scaling factors for time, pressure and kinematic viscosity can be evaluated as $s_t = s_l s_v^{-1}$, $s_p = s_\rho s_v^2$, $s_\nu = s_l^2 s_t^{-1}$, respectively.

It should be pointed out that accuracy and stability of any run depend on the selection of these scaling factor. In fact, the LBM recovers the solution of the incompressible Navier-Stokes equations in the limit of vanishing Mach number. In other words, the lower the velocity in LB units, the more accurate the solution is. In addition, high values of the Mach number of the simulations can lead to unstable runs. Moreover, the fluid kinematic viscosity $\nu = \tau c_s^2$ in lattice units should correspond to $\tau + \frac{1}{2} \in \left(\frac{1}{2} : 1\right]$, with the stability decreasing as $\nu \to 0$.